Perturbative Born theory for light scattering by time-modulated scatterers

Dionysios Galanis,[1,2] Evangelos Almpanis,[1] Nikolaos Papanikolaou,[1] and Nikolaos Stefanou[2]

[1] *Institute of Nanoscience and Nanotechnology, NCSR "Demokritos", Patriarchou Gregoriou and Neapoleos Str., Ag. Paraskevi, Athens GR-153 10, Greece*

[2] *Section of Condensed Matter Physics, National and Kapodistrian University of Athens, University Campus, GR-157 84 Athens, Greece*

(Dated: April 20, 2026)

We present a theoretical framework for electromagnetic scattering by particles with a permittivity that is periodically varying in time, based on a perturbative approach. Within this framework, we derive explicit expressions for the scattering matrix of the dynamic system in a first-order Born approximation, relating it directly to the corresponding static problem. We show that inelastic scattering amplitudes are governed by overlap integrals between static modes at the input and output frequencies. Using this insight, we analyze scattering from a time-modulated, isotropic, dielectric sphere and a high-permittivity dielectric cylinder, and demonstrate how modal orthogonality can suppress inelastic channels, while appropriate tuning of geometric parameters can significantly enhance them. In particular, we show that cylindrical resonators support strong inelastic scattering when resonance-to-resonance optical transitions, induced by the temporal variation, involve a high-Q supercavity mode. Comparison with full time-Floquet calculations confirms that the first-order Born approximation remains quantitatively accurate for modest modulation amplitudes and provides clear physical intuition for frequency conversion and resonance-mediated scattering processes in time-modulated photonic resonators.

arXiv:2601.23003v2 [physics.optics] 20 Apr 2026

I. INTRODUCTION

The ability to control light in both space and time has opened new avenues in optics and photonics, enabling functionalities that go beyond those of the respective static systems. Although the study of time-modulated electromagnetic media dates back to the 1950s and 1960s [1, 2], it has only recently gained renewed attention thanks to advances in modern experimental and nanofabrication techniques. Temporal modulation in photonic systems enables a wide range of applications, including nonreciprocal propagation of light without the need of magnetic materials [3], frequency conversion using linear materials [4], parametric amplification [5, 6], and the realization of photonic time crystals (systems with wavevector gaps) [7]. Beyond these fundamental effects, time-modulated photonic platforms have been proposed for more sophisticated applications, ranging from the creation of synthetic dimensions and the exploration of topological phases [8] to photonic analogs of the Aharonov–Bohm effect [9], temporal Wood anomalies [10], extension of the Smith-Purcell effect into the fourth dimension [11] and the optical equivalent of Fresnel drag [12]. An extensive list of possible applications of time-modulated electromagnetic media can be found in Refs. [13–19].

From a fundamental perspective, complex electromagnetic structures can be regarded as assemblies of elementary building blocks, each corresponding to a single scatterer. Such time-modulated scatterers constitute the essential ingredients of dynamically reconfigurable photonic systems, and their study provides valuable physical insight that remains only partially explored. Typical examples include particles with a time-varying permittivity [20–23] or geometrical deformation [24], where the temporal variation may arise from electrical control [25], acoustic vibrations [26], spin-wave excitations [27, 28], or even in an all-optical manner using the nonlinear Kerr effect [29]. Transparent conductive oxides also offer a promising avenue for all-optical time-variation using ultrashort laser pulses [30, 31]. The temporal modulation of a scatterer couples different frequency components of the electromagnetic field, leading to the generation of frequency sidebands while the energy of the optical system is not conserved, since energy exchange with the external modulation source is allowed. Depending on the modulation strength and frequency, rich physical behavior can emerge, including asymmetric scattering spectra, enhanced forward or backward scattering, and effective gain or loss associated with the modulation process.

In order to provide a versatile and computationally efficient description of time-modulated optical scatterers, we develop here a perturbative Born theory in which the temporal variation of the material permittivity is treated as a small parameter, as is relevant for realistic applications. This approach enables a systematic evaluation of the coupling between frequency components induced by the variation, while retaining the full spatial dependence of the scattering problem. Within this formalism, the electromagnetic fields are expanded in harmonics of the modulation frequency, and the first-order correction terms naturally describe processes such as frequency conversion and modulation-induced asymmetry in the scattering pattern. Unlike previous, more accurate, descriptions using time-Floquet expansions [20, 23] or fully numerical finite-difference time-domain (FDTD) [32] simulations, the perturbative treatment provides direct physical insight into the mechanisms governing optical transitions between modes and yields closed-form expressions for the sideband amplitudes. Moreover, it can be

readily incorporated into existing multiple-scattering or modal-expansion frameworks [3, 33, 34], thereby bridging detailed models of individual dynamic scatterers with macroscopic time-modulated photonic structures.

The remainder of the paper is organized as follows. Section II presents a theoretical framework for modeling scattering from bodies with periodically varying permittivity, based on a perturbative approach and, for practical implementations, restricted to the first-order Born approximation. Section III compares this approximation with the dynamic Extended Boundary Condition Method (EBCM) [23] and demonstrates that, at least for small modulation strengths, inelastic scattering amplitudes are governed by the overlap between static modes at the input and output frequencies. Both a dielectric sphere and a high-permittivity dielectric cylinder are treated as examples of inelastic scattering behavior with a particular focus on resonance-to-resonance optical transitions. Section IV summarizes the main conclusions of the work.

II. THEORETICAL METHODS

In this section, we present a theoretical method for light scattering by a single particle with a permittivity that varies periodically in time, employing a perturbative approach and deriving the scattering T matrix within the first-order Born approximation. For completeness and comparison, we first provide a brief review of the full time-Floquet method developed previously for spherical scatterers [20, 24] and scatterers of general shape [23].

A. Time-Floquet method

We consider a finite scatterer occupying volume $V_{\rm in}$, made of a homogeneous and isotropic material with permeability $\mu\mu_0$ and periodically varying permittivity $\varepsilon(t)\varepsilon_0$ surrounded by a homogeneous, isotropic and time-independent medium with permeability $\mu_{\rm h}\mu_0$ and permittivity $\varepsilon_{\rm h}\varepsilon_0$. Due to Floquet's theorem [35], any solution of Maxwell's equations can be written as a superposition of Floquet solutions of the form

$$\mathbf{E}(\mathbf{r},t) = \mathrm{e}^{-i\omega t}\sum_n \mathbf{E}_n(\mathbf{r})\mathrm{e}^{in\Omega t}, \tag{1}$$

where ω is the Floquet quasifrequency, Ω is the modulation frequency, and the sum extends over all integers. The magnetic field can be expanded similarly. Then, we expand each divergence-less $\mathbf{E}_n(\mathbf{r})$ in transverse vector spherical waves.

Away from the scatterer, the field is expanded as

$$\mathbf{E}_n^{\rm out}(\mathbf{r}) = \mathbf{E}_n^{\rm inc}(\mathbf{r}) + \mathbf{E}_n^{\rm sc}(\mathbf{r}), \tag{2}$$

which is the sum of an incoming field, typically a plane wave,

$$\mathbf{E}_n^{\rm inc}(\mathbf{r}) = \sum_L a_{Ln}^{\rm inc}\,\mathbf{J}_L(q_{{\rm h}n},\mathbf{r}), \tag{3}$$

and the scattered field

$$\mathbf{E}_n^{\rm sc}(\mathbf{r}) = \sum_L a_{Ln}^{\rm sc}\,\mathbf{H}_L(q_{{\rm h}n},\mathbf{r}), \tag{4}$$

where

$$q_{{\rm h}n} = \frac{\sqrt{\mu_{\rm h}\varepsilon_{\rm h}}}{c}(\omega - n\Omega) = \sqrt{\mu_{\rm h}\varepsilon_{\rm h}}k_n, \tag{5}$$

c being the velocity of light in vacuum, while L is a shorthand index for the indices ℓ, m and polarization modes $P = E, H$. As in Ref. [23], $\mathbf{J}_{H\ell m}(q_{{\rm h}n},\mathbf{r}) = j_\ell(q_{{\rm h}n}r)\mathbf{X}_{\ell m}(\widehat{\mathbf{r}})$ and $\mathbf{J}_{E\ell m}(q_{{\rm h}n},\mathbf{r}) = \frac{i}{q_{{\rm h}n}}\nabla\times\mathbf{J}_{H\ell m}(q_{{\rm h}n},\mathbf{r})$ are the regular transverse vector spherical waves, $j_\ell(x)$ are the spherical Bessel functions, $\mathbf{X}_{\ell m}(\widehat{\mathbf{r}})$ are the vector spherical harmonics and $\mathbf{H}_L(q_{{\rm h}n},\mathbf{r})$ are the outgoing transverse vector spherical waves, obtained by replacing $j_\ell(q_{{\rm h}n}r)$ in $\mathbf{J}_L(q_{{\rm h}n},\mathbf{r})$ with the spherical Hankel function of the first kind $h_\ell^+(q_{{\rm h}n}r)$. We emphasize that $\mathbf{H}_L$ should not be confused with the magnetic field $\mathbf{H}$, as its meaning is clear from the context. Inside the scatterer, the field $\mathbf{E}_n^{\rm in}$ can also be expanded in transverse vector spherical waves, as detailed in Ref. [20].

Due to the linearity of Maxwell's equations, the coefficients $a_{Ln}^{\rm inc}$ and $a_{Ln}^{\rm sc}$ are linearly dependent, and we define the T matrix as

$$a_{Ln}^{\rm sc} = \sum_{L',n'} T_{Ln;L'n'}\,a_{L'n'}^{\rm inc}. \tag{6}$$

The T matrix can be efficiently calculated for finite scatterers close to a spherical shape using the dynamic EBCM by invoking the continuity of the components of the electric and magnetic fields parallel to the scatterer's surface

$$\widehat{\mathbf{n}}\times\mathbf{E}_n^{\rm in} = \widehat{\mathbf{n}}\times\mathbf{E}_n^{\rm out}, \tag{7a}$$

$$\widehat{\mathbf{n}}\times\mathbf{H}_n^{\rm in} = \widehat{\mathbf{n}}\times\mathbf{H}_n^{\rm out}. \tag{7b}$$

Details of the derivation are given in Ref. [23]. In the end, the T matrix is given by a system of linear equations

$$\sum_{L''n''} T_{Ln;L''n''}Q^0_{L''n'';L'\nu} = -Q^+_{Ln;L'\nu}. \tag{8}$$

Explicit expressions for the matrix elements $Q^{0/+}_{Ln;L'\nu}$ are given in Ref. [23]. This system of linear equations can be solved numerically by introducing cutoffs in indices ℓ and n. The static case is retrieved by imposing a cutoff in the Floquet components equal to $n = 0$. Solving for the transposed matrices improves numerical stability [36].

B. Perturbative approach

We now proceed with a perturbative approach to evaluate the T matrix. We consider the same finite scatterer as

in Subsection II A with periodically varying permittivity. From Maxwell's equations in the absence of sources,

$$\nabla \times \mathbf{E}(\mathbf{r},t) = -\frac{\partial}{\partial t}\mathbf{B}(\mathbf{r},t), \tag{9a}$$

$$\nabla \times \mathbf{H}(\mathbf{r},t) = \frac{\partial}{\partial t}\mathbf{D}(\mathbf{r},t), \tag{9b}$$

it can be shown that the electric field both inside and outside the scatterer satisfies

$$\nabla \times \frac{1}{\mu(\mathbf{r})}\nabla \times \mathbf{E}_n(\mathbf{r}) = \left(\frac{\omega - n\Omega}{c}\right)^2 \sum_{n'} \varepsilon_{n-n'}(\mathbf{r})\mathbf{E}_{n'}(\mathbf{r}), \tag{10}$$

where ε and μ are allowed to vary spatially, and the Fourier transform

$$\varepsilon(\mathbf{r},t) = \sum_n \varepsilon_n(\mathbf{r})\mathrm{e}^{in\Omega t}, \tag{11a}$$

$$\varepsilon_n(\mathbf{r}) = \frac{1}{T}\int_0^T \varepsilon(\mathbf{r},t)\mathrm{e}^{-in\Omega t}\,\mathrm{d}t \tag{11b}$$

has been taken.

The first-order Born approximation is extracted from Eq. (10) by treating the static case as the unperturbed system and the variation as the perturbation. To be more specific, writing

$$\varepsilon_n(\mathbf{r}) = \varepsilon^{(0)}(\mathbf{r})\delta_{n0} + \Delta\varepsilon_n(\mathbf{r}), \tag{12}$$

we have

$$\begin{aligned}&\nabla \times \frac{1}{\mu(\mathbf{r})}\nabla \times \mathbf{E}_n(\mathbf{r}) - k_n^2\varepsilon^{(0)}(\mathbf{r})\mathbf{E}_n(\mathbf{r})\\ &= k_n^2 \sum_{n'} \Delta\varepsilon_{n-n'}(\mathbf{r})\mathbf{E}_{n'}(\mathbf{r}).\end{aligned} \tag{13}$$

We now introduce the dyadic Green's function $\overleftrightarrow{G}_0(k,\mathbf{r},\mathbf{r}')$ for the static scatterer,

$$\left(k^2\varepsilon^{(0)}(\mathbf{r}) - \nabla \times \frac{1}{\mu(\mathbf{r})}\nabla\times\right)\overleftrightarrow{G}_0(k,\mathbf{r},\mathbf{r}') = \overleftrightarrow{I}\,\delta(\mathbf{r}-\mathbf{r}'). \tag{14}$$

This function can be shown [37, 38] to be equal to

$$\overleftrightarrow{G}_0(k,\mathbf{r},\mathbf{r}') = -iq_\mathrm{h}\mu_\mathrm{h}\sum_L \mathbf{I}_L(k,\mathbf{r}) \otimes \overline{\mathbf{R}}_L(k,\mathbf{r}'), \quad r > r', \tag{15}$$

where $\mathbf{I}_L(k,\mathbf{r})$ is the irregular solution, equal to an outgoing wave $\mathbf{H}_L(q_\mathrm{h},\mathbf{r})$ outside the sphere, while $\overline{\mathbf{R}}_L(k,\mathbf{r})$ is the regular solution, obtained by the scattering of an incoming wave $\overline{\mathbf{J}}_L(q_\mathrm{h},\mathbf{r})$. The *bar* operation on a vector spherical wave is defined as follows [23]

$$\overline{\mathbf{F}}_{H\ell m} = f_\ell \mathbf{X}^*_{\ell m} = (-1)^{m+1}\mathbf{F}_{H\ell -m}, \tag{16a}$$

$$\overline{\mathbf{F}}_{E\ell m} = -\frac{i}{q}\nabla \times (f_\ell \mathbf{X}^*_{\ell m}) = (-1)^m \mathbf{F}_{E\ell -m}, \tag{16b}$$

where F can refer to Bessel or Hankel vector spherical waves, while f, correspondingly, refer to the spherical Bessel or Hankel functions. Moreover, if we introduce an integer index p such that

$$P = E \Leftrightarrow p = 0, \qquad P = H \Leftrightarrow p = 1, \tag{17}$$

and the *bar* operation on index L such that

$$L = P\ell m \Leftrightarrow \overline{L} = P, \ell, -m, \tag{18}$$

we can write the definition more compactly as

$$\overline{\mathbf{F}}_L = (-1)^{m+p}\mathbf{F}_{\overline{L}}. \tag{19}$$

By virtue of the Green's function and Eq. (13), we obtain a Lippmann-Schwinger equation,

$$\begin{aligned}&\mathbf{E}_n(\mathbf{r}) = \mathbf{E}_n^{(0)}(\mathbf{r})\\ &- \int k_n^2 \overleftrightarrow{G}_0(k_n,\mathbf{r},\mathbf{r}') \sum_{n'} \Delta\varepsilon_{n-n'}(\mathbf{r}')\mathbf{E}_{n'}(\mathbf{r}')\,\mathrm{d}^3r',\end{aligned} \tag{20}$$

with $\mathbf{E}_n^{(0)}$ being a scattering solution of the static system.

To calculate the T matrix, we consider an incoming vector spherical wave $\mathbf{J}_L(q_{\mathrm{h}n},\mathbf{r})$ of frequency $\omega - n\Omega$, so that in the perturbed system we have

$$\begin{aligned}\mathbf{E}_{n'}(\mathbf{r}) =& \mathbf{J}_L(q_{\mathrm{h}n},\mathbf{r})\delta_{nn'}\\ &+ \sum_{L'} T_{L'n',Ln}\mathbf{H}_{L'}(q_{\mathrm{h}n'},\mathbf{r}), \quad r > r_>,\end{aligned} \tag{21}$$

$r_>$ being the radius of the smallest circumscribing sphere of the scatterer, centered at the origin of our coordinate system [36]. On the other hand, the corresponding solution, $\mathbf{E}_n^{(0)}$, for the unperturbed system is the regular solution $\mathbf{R}_L(k_n,\mathbf{r})$ as in Eq. (15) (but without the bar)

$$\begin{aligned}\mathbf{E}_n^{(0)}(\mathbf{r}) &= \mathbf{R}_L(k_n,\mathbf{r})\\ &= \begin{cases}\mathbf{J}_L(q_\mathrm{hn},\mathbf{r})\\ \quad + \sum_{L'} T^{(0)}_{L'L}(k_n)\mathbf{H}_{L'}(q_\mathrm{hn},\mathbf{r}), & r > r_>\\ \sum_{L'} \alpha_{L'L}(k_n)\mathbf{J}_{L'}(q_n,\mathbf{r}), & \mathbf{r} \in V_\mathrm{in}\end{cases},\end{aligned} \tag{22}$$

with $\mathbf{E}_{n'}^{(0)} = 0$ for $n' \neq n$, and $q_n = k_n\sqrt{\mu\varepsilon}$. Substituting $\overline{L}$ for L in Eq. (22), using Eq. (19) and invoking the uniqueness of solutions of Maxwell's equations, we obtain

$$\begin{aligned}\overline{\mathbf{R}}_L(k_n,\mathbf{r}) &= (-1)^{m+p}\mathbf{R}_{\overline{L}}(k_n,\mathbf{r})\\ &= \begin{cases}\overline{\mathbf{J}}_L(q_\mathrm{hn},\mathbf{r})\\ \quad + \sum_{L'} \overline{T}^{(0)}_{L'L}(k_n)\mathbf{H}_{L'}(q_\mathrm{hn},\mathbf{r}), & r > r_>\\ \sum_{L'} \overline{\alpha}_{L'L}(k_n)\mathbf{J}_{L'}(q_n,\mathbf{r}), & \mathbf{r} \in V_\mathrm{in}\end{cases},\end{aligned} \tag{23}$$

where

$$\overline{T}^{(0)}_{L'L}(k_n) = (-1)^{m+p}T^{(0)}_{L'\overline{L}}(k_n), \tag{24a}$$

$$\overline{\alpha}_{L'L}(k_n) = (-1)^{m+p}\alpha_{L'\overline{L}}(k_n). \tag{24b}$$

The first-order Born approximation consists in taking $\mathbf{E}_n = \mathbf{E}_n^{(0)}$ on the right hand side of Eq. (20). Taking into account Eqs. (15), (22) and (23), we get that, for r large enough,

$$\begin{aligned}\mathbf{E}_{n'}(\mathbf{r}) = &\left\{\mathbf{J}_L(q_{\mathrm{h}n},\mathbf{r}) + \sum_{L'} T^{(0)}_{L'L}(k_n)\mathbf{H}_{L'}(q_{\mathrm{h}n},\mathbf{r})\right\}\delta_{nn'} \\ &+ \sum_{L'}\mathbf{H}_{L'}(q_{hn'},\mathbf{r})\Big\{ i q_{hn'}\mu_h k_{n'}^2 \\ &\times \sum_{L'',L'''}\Big[\overline{\alpha}_{L''L'}(k_{n'})\alpha_{L'''L}(k_n) \\ &\times \int_{V_{\mathrm{in}}} \Delta\varepsilon_{n'-n}(\mathbf{r}')\mathbf{J}_{L''}(q_{n'},\mathbf{r}')\cdot\mathbf{J}_{L'''}(q_n,\mathbf{r}')\,\mathrm{d}^3r'\Big]\Big\}.\end{aligned} \tag{25}$$

Comparing Eq. (25) with Eq. (21), we finally obtain the first-order Born approximation for the T matrix (note the exchange of primed and unprimed indices)

$$\begin{aligned}T^{(1)}_{Ln;L'n'} =& i q_{\mathrm{h}n}^3 \int_{V_{\mathrm{in}}} \frac{\Delta\varepsilon_{n-n'}(\mathbf{r})}{\varepsilon_{\mathrm{h}}}\overline{\mathbf{R}}_L(k_n,\mathbf{r})\cdot\mathbf{R}_{L'}(k_{n'},\mathbf{r})\,\mathrm{d}^3r \\ =& i q_{\mathrm{h}n}^3 \sum_{L'',L'''}\Big\{\overline{\alpha}_{L''L}(k_n)\alpha_{L'''L'}(k_{n'}) \\ &\times \int_{V_{\mathrm{in}}} \frac{\Delta\varepsilon_{n-n'}(\mathbf{r})}{\varepsilon_{\mathrm{h}}}\mathbf{J}_{L''}(q_n,\mathbf{r})\cdot\mathbf{J}_{L'''}(q_{n'},\mathbf{r})\,\mathrm{d}^3r\Big\}.\end{aligned} \tag{26}$$

In the case of spatially homogeneous modulation inside the scatterer, $\Delta\varepsilon_{n-n'}$ can be extracted from the integral. However, keeping the integral in its general form is advantageous, as the perturbative approach—despite being approximate—allows one to treat spatially inhomogeneous modulations, contrary to the exact time-Floquet method outlined in Subsection II A.

It should be noted that the T matrix given by Eq. (26) is defined by the solutions of the static particle corresponding to incoming and outgoing waves with wavenumbers $q_{\mathrm{h}n}$ and $q_{\mathrm{h}n'}$, respectively. In general, the coefficients $\alpha_{L'''L'}(k_{n'})$ can be found by the static EBCM. By virtue of Eq. (24b), no extra effort is required to calculate $\overline{\alpha}_{L''L}(k_n)$. To reduce computational cost, the volume integral can be converted into a surface integral, as shown in Appendix A. An alternative way to derive the Born approximation for general Floquet media can be obtained by generalizing the analysis of Ref. [39].

C. Application for a sphere

In the case of a spherical scatterer of radius R, a full analytical result can be obtained. Since the expansion coefficients inside the sphere have the form $\alpha_{LL'} = \alpha_{P\ell}\delta_{LL'}$, we have

$$\mathbf{R}_L(k,\mathbf{r}) = \alpha_{P\ell}(k)\mathbf{J}_L(q,\mathbf{r}), \tag{27a}$$

$$\overline{\mathbf{R}}_L(k,\mathbf{r}) = \alpha_{P\ell}(k)\overline{\mathbf{J}}_L(q,\mathbf{r}), \tag{27b}$$

for $r < R$. Substituting $\overline{L}$ for L in Eq. (27a), by virtue of Eqs. (19) and (23), we get Eq. (27b). The expressions for the expansion coefficients inside the sphere, $\alpha_{P\ell}(k)$, are given in Appendix B. The overlap integral can also be given in a closed form, as shown in Appendix B. Therefore, for a spatially homogeneous modulation, the T matrix simplifies to

$$\begin{aligned}T^{(1)}_{Ln;L'n'} =& i q_{\mathrm{h}n}^3 \frac{\Delta\varepsilon_{n-n'}}{\varepsilon_{\mathrm{h}}}\int_{V_{\mathrm{in}}}\overline{\mathbf{R}}_L(k_n,\mathbf{r})\cdot\mathbf{R}_{L'}(k_{n'},\mathbf{r})\,\mathrm{d}^3r \\ =& i(q_{\mathrm{h}n}R)^3\frac{\Delta\varepsilon_{n-n'}}{\varepsilon_{\mathrm{h}}}\delta_{LL'} \\ &\times \alpha_{P\ell}(k_n)\alpha_{P\ell}(k_{n'})D_{P\ell}(q_nR,q_{n'}R),\end{aligned} \tag{28}$$

where the radial overlap integrals $D_{P\ell}$ are given in Appendix B. The $\delta_{L'L}$ term indicates that modes with different $L = P\ell m$ do not couple, which is a selection rule, in the case of time-modulated isotropic spheres, for the permittivity-variation induced Mie-mode-to-Mie mode coupling. The same selection rule results, also, from group-theoretical arguments. Since the symmetry of the Mie modes of the spherical particle is that of the $O(3)$ Lie group, and the temporal perturbation is an irreducible tensor operator which has the symmetry of the $D_{\mathrm{g}}^{(\ell=0)}$ irreducible representation of $O(3)$, then the perturbation operating on an eigenvector of the $P\ell$ irreducible subspace, transforms according to the relevant direct product representation: $D_{\mathrm{g}}^{(\ell=0)} \otimes D_{\mathrm{g,u}}^{(\ell)} = D_{\mathrm{g,u}}^{(\ell)}$. This implies a straightforward selection rule, according to which Mie-mode-to-Mie mode photonic transitions conserve both the angular momentum ℓ and the parity $\sigma = \mathrm{g},\mathrm{u}$ or, equivalently, the polarization of the mode.

For particles of revolution that possess a mirror plane perpendicular to the symmetry axis, such as spheroids or cylinders, the continuous rotational symmetry is reduced from $O(3)$ to $D_{\infty h}$, and the spherical Mie modes are split accordingly [40]. In this case, the eigenmodes are classified according to the irreducible representations of the $D_{\infty h}$ group, labeled by $|m|$ and parity $\sigma = \mathrm{g},\mathrm{u}$. As for the sphere, successive solutions within each irreducible subspace are indexed by the radial order. Mode-to-mode transitions are allowed only between eigenmodes belonging to the same irreducible subspace but with different radial orders.

D. Cross sections

In order to derive observable quantities from the T matrix, such as absorbed or scattered power, we need to calculate the Poynting vector $\mathbf{S}$. In particular, we consider the temporal mean value $\frac{1}{T}\int_0^T \mathrm{d}t$ over a very long time interval $T \to \infty$, and then integrate over the surface of a sphere $S^2(r)$, $r \to \infty$, that surrounds the scatterer to obtain outgoing power. From there, one can define normalized scattering and absorption cross sections [23].

For an incident plane wave of unit amplitude

$$\mathbf{E}^{\rm inc}(\mathbf{r},t) = {\rm e}^{-i(\omega-p\Omega)t}{\rm e}^{iq_{\rm hp}\widehat{\mathbf{k}}\cdot\mathbf{r}}\widehat{\mathbf{p}} = {\rm e}^{-i(\omega-p\Omega)t}\sum_L a^{\rm inc}_{Lp}\mathbf{J}_L(q_{\rm hp},\mathbf{r}), \tag{29}$$

we get the (normalized) scattering cross section,

$$\sigma^{\rm sc} = \sum_n \sigma^{\rm sc}_n = \frac{1}{\pi}\sum_{n,L}\frac{1}{(q_{\rm hn}R_{\rm eff})^2}|a^{\rm sc}_{Ln}|^2, \tag{30}$$

and the absorption cross section,

$$\sigma^{\rm abs} = \sigma^{\rm ext} - \sigma^{\rm sc}, \tag{31}$$

where the extinction cross section is defined as

$$\sigma^{\rm ext} = -\frac{1}{\pi}\sum_L \frac{1}{(q_{\rm hp}R_{\rm eff})^2}{\rm Re}\left[(a^{\rm inc}_{Lp})^* a^{\rm sc}_{Lp}\right]. \tag{32}$$

The effective radius $R_{\rm eff}$ is an arbitrary normalization quantity. In Ref. [23], it is defined as the radius of a sphere with the same volume as the scatterer. Here, we adopt a different convention: for spherical scatterers, $R_{\rm eff}$ is taken to be the sphere radius, while for cylindrical scatterers, it is taken to be the cylinder radius. In the case of spheres, the scattering cross section takes a simpler form [20]

$$\sigma^{\rm sc} = \sum_n\sum_{Pl}\sigma^{\rm sc}_{P\ell n} = \sum_n \frac{2}{(q_{\rm hn}R_{\rm eff})^2}\sum_{Pl}(2l+1)|T_{P\ell;np}|^2, \tag{33}$$

where $T_{P\ell;np}$ is the, diagonal with respect to L, element of the T matrix. Most results in the following are given in terms of those cross sections.

III. RESULTS AND DISCUSSION

Recent advances in low-loss metaphotonic platforms have concentrated on all-dielectric structures supporting Mie-type resonances [41]. Dynamic control through temporal modulation of such structures has further enabled the engineering of inter-resonance coupling [42]. Efficient inelastic scattering in resonant systems requires substantial spatial overlap between the electromagnetic fields at the incoming and outgoing frequencies. This requirement can be met by using tightly confined, symmetry-matched modes, especially when both frequencies correspond to resonant states of the structure [43–45].

Although the scattering T matrix formalism has previously been applied to particles with periodic time-modulation, a simplified Born approximation framework can offer valuable physical insight and guide the optimization of inelastic scattering processes. Here, we apply this approach to two geometries: a dielectric sphere, for which the Born approximation admits an analytical solution, and a dielectric cylinder, which requires a numerical treatment based on Eq. (26). For the cylindrical case, we specifically investigate inelastic scattering mediated by a so-called *supercavity* mode [46].

A. Dielectric sphere

Light scattering from dielectric spheres with harmonically varying permittivity or radius, at frequencies in the vicinity of a Mie resonance, has been analyzed in previous studies [3, 20, 24]. The presence of a resonance can significantly enhance the generated harmonics and induce asymmetries between the Stokes and anti-Stokes components. Such asymmetries enable an exchange of energy between the optical field and the external mechanism responsible for driving the periodic permittivity variation.

Figure 1a shows the scattering cross section of a linearly polarized plane wave incident on a static dielectric sphere of radius R, relative permittivity $\varepsilon = 12$, and permeability $\mu = 1$. The spectral response exhibits prominent contributions from Mie resonances, each characterized by its angular momentum index ℓ and polarization (electric or magnetic). As energy increases, resonances associated with higher ℓ values emerge, along with higher-order radial modes for a given ℓ. The resulting spectral overlap leads to a rich optical spectrum. As discussed above, the spherical symmetry of the system prevents coupling between modes of different ℓ under a uniform time-periodic variation of the permittivity. Therefore, we restrict our analysis to the first two resonances for $\ell = 2$, denoted QM_1 and QM_2 in Fig. 1a. The individual contribution of only the quadrupolar ($\ell = 2$) modes of magnetic type ($P = H$) is shown in Fig. 1a by the dashed line. The imaginary part of the E_y component for QM_1 and QM_2 is also depicted on the right-hand side of Fig. 1 as it provides the dominant contribution to the electric field for both modes.

Next, we introduce a uniform harmonic variation of the permittivity of the sphere of the form

$$\varepsilon(t) = \varepsilon_0\varepsilon[1+\eta\cos(\Omega t)] \tag{34}$$

and examine the first, Stokes and anti-Stokes, inelastic components $n = \pm 1$ (with frequencies $\omega \mp \Omega$) of the scattering cross section. The scattering cross section for incoming frequency on resonance QM_1 is shown in Figs. 1(b, c), as we vary the modulation frequency Ω, for two modulation amplitudes η. Both the full dynamic calculation (full lines) and the Born approximation (dashed lines) results are displayed. The Born approximation works very well for moderate modulation amplitudes ($\eta = 0.01$), while for larger amplitudes ($\eta = 0.1$) only near the adiabatic limit—that is, for small Ω—we observe a significant divergence.

The incoming frequency is chosen on resonance QM_1 to maximize the field corresponding to the input frequency in the overlap integral, thereby enhancing the inelastic scattering. By applying the same logic to the field corresponding to the output frequency, we expect stronger inelastic effects when the outgoing frequency lies within the same resonance halfwidth, or corresponds to another resonance with the same angular symmetry (P, ℓ) but a different radial order. This likely explains the divergence

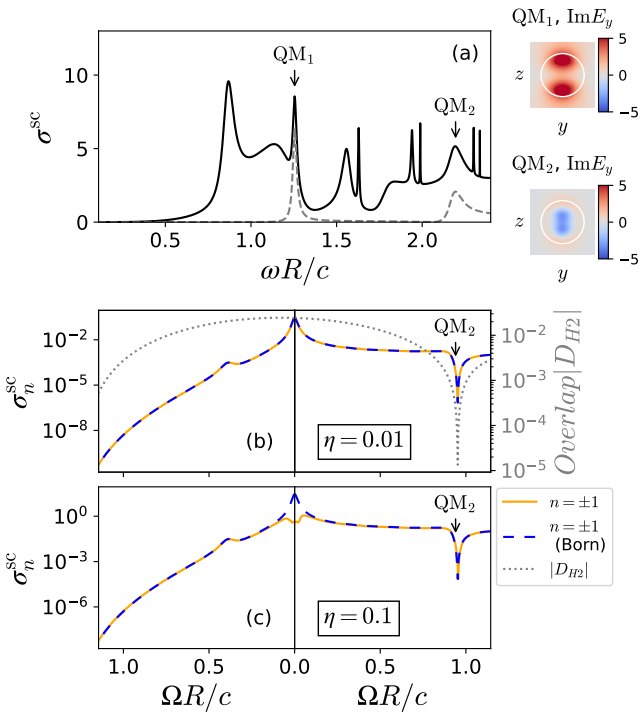

FIG. 1. Light scattering by a sphere of radius R with static permittivity $\varepsilon = 12$ and permeability $\mu = 1$. Spherical waves up to $\ell_{\max} = 5$ have been retained. (a): Static scattering cross section of a plane wave, incident along the x direction, calculated by the static EBCM (solid line), and its $P\ell = H2$ component (dashed line). We can see two resonances, QM$_1$ and QM$_2$, corresponding to $P\ell = H2$, in the displayed spectral region. In the margin, we show the imaginary part of the y component of the electric field on the y-z section passing through the center of the sphere, for scattering at these resonances. (b): First inelastic ($n = \pm 1$) scattering cross section components for incoming frequency on resonance QM$_1$, as we vary the modulation frequency. The right (left) parts correspond to $n = -1$ ($n = 1$). The full (dashed) lines show the dynamic EBCM (Born approximation) results. A sharp dip for $n = -1$ is clearly visible. The dotted line depicts the absolute value of the radial overlap integral $|D_{H2}|$ from Eq. (B6). (c): Same as (b), but with higher modulation amplitude.

observed in the adiabatic limit: a resonance overlaps most strongly with itself, lowering the threshold at which higher-order phenomena can no longer be neglected.

The most intense inelastic phenomena are indeed observed in the adiabatic limit and when the modulation frequency lies within the Mie resonance halfwidth. However, when the modulation frequency approaches the frequency difference $\omega_{\mathrm{QM}_2} - \omega_{\mathrm{QM}_1}$, we observe a pronounced reduction in the corresponding inelastic scattering cross section, contrary to the intuitive expectation of enhancement. This dip can be understood within the Born approximation and arises from a node in the radial overlap integral D_{H2} that enters Eq. (28), which is shown in Fig. 1b by the dotted line. Such a node is expected from the field profiles shown in Fig. 1 for incident plane waves. For the QM$_1$ resonance the sign of ImE_y—the dominant electric-field component, as noted above—remains constant, while for QM$_2$ it changes sign near the sphere boundary. Consequently, their overlap integral largely cancels. This overlap integral should approximate D_{H2}, since on resonance the scattering is dominated by spherical waves with $P\ell = H2$.

It is noteworthy that the overlap integral of the two modes with different radial order is found to vanish for modulation frequencies slightly offset from $\Omega = \omega_{\mathrm{QM}_2} - \omega_{\mathrm{QM}_1}$. This is most likely due to the fact that the temporal variation shifts the resonances of the time-modulated system with respect to those of the static system. This shift is best explained through the framework of quasinormal mode theory [47, 48] or resonant state expansion [39]. Both approaches focus on the *complex* eigenfrequencies and the corresponding eigenfields of Maxwell's equations in an open system, and allow for the calculation of resonance frequencies of a perturbed system from the resonances of a background system — the former through coupled mode theories [47, 49, 50] and the latter immediately, through a Mittag-Leffler expansion of the background Green's function. In both cases, the perturbation causes the resonances to move in the complex plane, which is sufficient to explain the effect observed here. Although both theories have been developed for static systems, a rather recent work [51] generalizes the resonant state expansion to time-modulated Floquet systems. As described there, Floquet's theorem implies that each static resonance generates a series of *replicas*, shifted by integer multiples of the modulation frequency Ω. The integer n labels these Floquet harmonics, with $n = 0$ corresponding to the original static resonance. In the absence of modulation, replicas with different n are uncoupled. Modulation, however, induces interactions between them. In resonance-to-resonance transitions, the real frequency of one static resonance coincides with the $n = \pm 1$ replica of another, facilitating their interaction and likely causing the observed shift.

The suppression of harmonic modes is also observed for other pairs of resonances sharing the same angular momentum and polarization, but different radial order. However, in dielectric spheres, the permittivity modulation frequencies required to induce these effects are relatively high, being comparable to the frequencies of the Mie resonances themselves. This imposes significant practical limitations, as achieving permittivity variations on the order of several terahertz remains challenging.

B. Dielectric cylinder

To investigate analogous phenomena at modulation frequencies substantially lower than the frequency of the electromagnetic wave, and to further explore the potential of resonance-to-resonance transitions, we turn our attention to a cylindrical scatterer. In this geometry, an

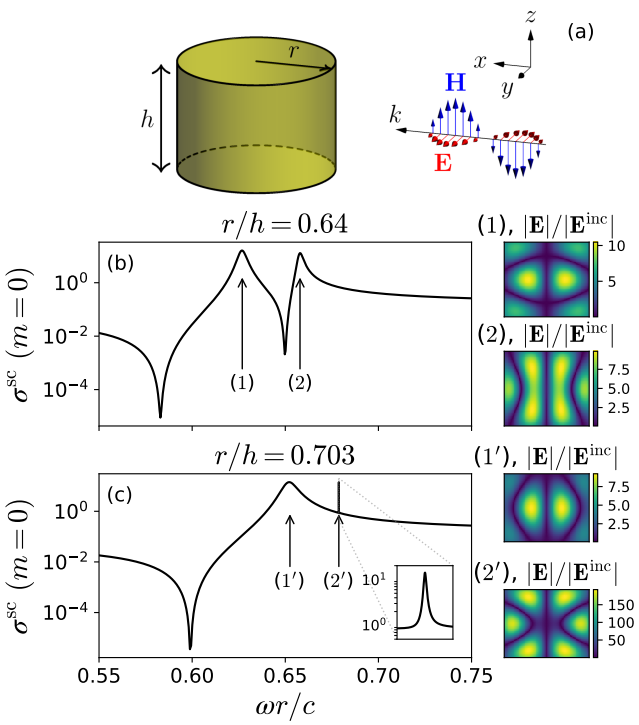

FIG. 2. (a): Cylindrical scatterer with $\varepsilon = 80$ and $\mu = 1$, of radius r and height h, illuminated by an s-polarized plane wave perpendicular to the cylinder axis. (b) and (c): Static scattering cross sections ($m = 0$ component) for two different cylinder aspect ratios, plotted as a function of the dimensionless frequency $\omega r/c$. The results are obtained using the static EBCM with angular-momentum cutoffs $\ell_{\max} = 10$ and $\ell_{\text{cut}} = 12$ [23]. The four resonances indicated by arrows occur at: $\omega r/c = 0.6269$ (1), $\omega r/c = 0.6579$ (2), $\omega r/c = 0.6525$ (1′), and $\omega r/c = 0.67875$ (2′). Resonance (2′) corresponds to the supercavity mode. The normalized electric-field distribution inside the cylinder in the y-z plane, perpendicular to the incident direction x, is shown in the margin for each resonance.

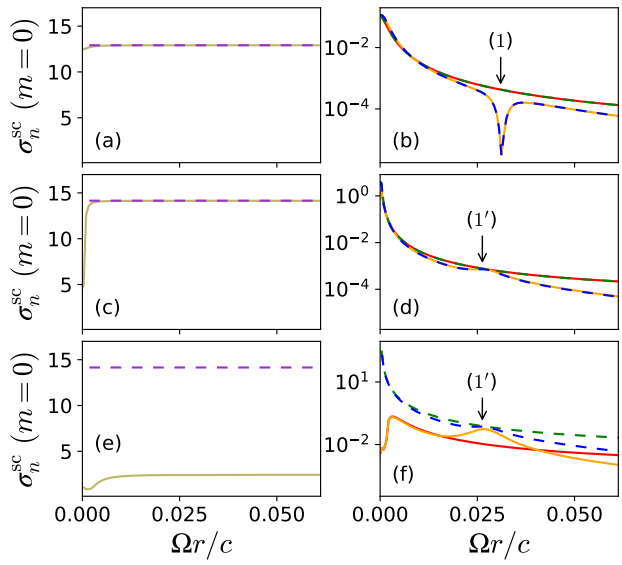

FIG. 3. Elastic ($n = 0$) and first inelastic ($n = \pm 1$) $m = 0$ components of the scattering cross section for the two different aspect ratios shown in Fig. 2. We consider an incoming plane wave with frequency corresponding to resonances (2) and (2′), respectively, and vary the dimensionless modulation frequency $\Omega r/c$. (a): $r/h = 0.64$, $n = 0$, $\eta = 0.001$. (b): $r/h = 0.64$, $n = \pm 1$, $\eta = 0.001$. (c): $r/h = 0.703$, $n = 0$, $\eta = 0.001$. (d): $r/h = 0.703$, $n = \pm 1$, $\eta = 0.001$. (e): $r/h = 0.703$, $n = 0$, $\eta = 0.01$. (f): $r/h = 0.703$, $n = \pm 1$, $\eta = 0.01$. The full (dashed) lines show the dynamic EBCM (Born approximation) results. For the figures on the right, the red and green curves show $n = -1$, while the orange and blue curves show $n = +1$. It can be seen that, for $r/h = 0.703$, a peak appears when we have resonance-to-resonance transition; that is, when the modulation frequency is such that the $n = 1$ component corresponds to resonance (1′). On the contrary, for $r/h = 0.64$ a sharp dip appears when the $n = 1$ component corresponds to resonance (1).

additional degree of freedom, the aspect ratio, enables closer spacing of resonances and allows for controlled modification of their modal profiles.

We consider a cylinder of radius r, height h, and permittivity $\varepsilon = 80$, as described in Ref. [46], and examine the scattering of an s-polarized plane wave, incident perpendicular to the symmetry axis of the cylinder, as shown in Fig. 2a. The component $m = 0$ of the scattering cross section is depicted in Figs. 2(b, c), for two different aspect ratios, $r/h = 0.64$ and $r/h = 0.703$, respectively. The two resonances, labeled (1) and (2) in Fig. 2b for $r/h = 0.64$, move closer together as the aspect ratio increases and, at $r/h = 0.703$, the supercavity mode, denoted as resonance (2′), is formed, as demonstrated in Ref. [46].

We next introduce, as before, a time-variation of the permittivity of the cylinder in the form of Eq. (34), and study the scattering of incoming plane waves with frequencies on resonance (2) or (2′). The Stokes and anti-Stokes components $n = \pm 1$ of the scattering cross section are depicted in Fig. 3, along with the elastic ($n = 0$) component, which serves as a further test of the validity of Born approximation.

In the adiabatic limit, the system is anticipated to exhibit the most pronounced inelastic phenomena. Furthermore, the transition between selected resonances, induced by a harmonic permittivity variation, is fundamentally governed by the overlap integral between the respective mode profiles. This is indeed confirmed by the results shown in Fig. 3. For an aspect ratio $r/h = 0.64$, the $n = 1$ (Stokes) component of the scattering cross section (Fig. 3b) exhibits a sharp dip at $\Omega \approx \omega_2 - \omega_1$. In contrast, for $r/h = 0.703$, when the modulation frequency matches the frequency difference between resonances (2′) and (1′) (see Fig. 3d), the destructive interference is suppressed, leading to a broad peak of moderate intensity. Since the Born approximation accurately reproduces the exact results for a modulation amplitude $\eta = 0.001$, this behavior should be attributed to a modification of the modal overlap. This reconfiguration arises from the strong

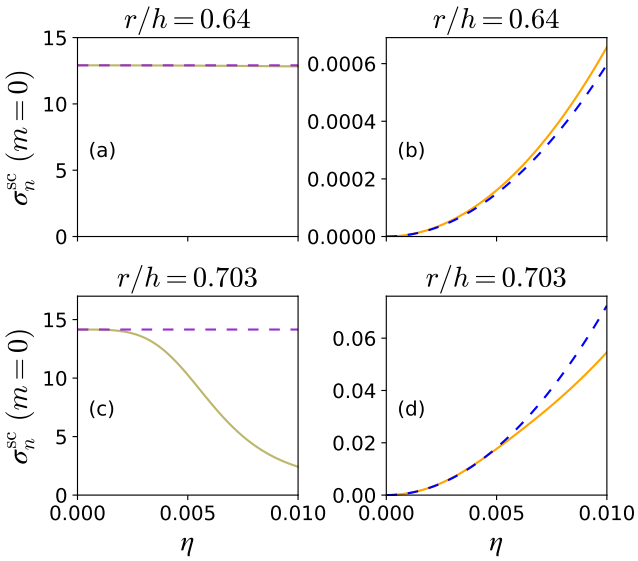

FIG. 4. Elastic ($n = 0$, left-hand diagrams) and inelastic ($n = 1$, right-hand diagrams) components of the scattering cross section as a function of the modulation amplitude η for the transitions (2) $\to$ (1) and (2′) $\to$ (1′), manifested in the right-hand diagrams of Fig. 3. The full (dashed) lines show the dynamic EBCM (Born approximation) results. For both aspect ratios, the Born approximation breaks down at sufficiently large η.

interaction between resonances.

For $r/h = 0.703$ and $\eta = 0.01$, the Born approximation is no longer reliable as evidenced from Figs. 3(e, f). However, the peak just above $\Omega r/c = 0.025$ still survives and almost surpasses the inelastic cross section for $\Omega \to 0$. Transitions between resonances are difficult to achieve in Floquet systems with single symmetric particles, such as spheres or cylinders. However, stronger modulation or alternative geometries, for instance collections of particles, can produce pronounced resonance-to-resonance transitions, as predicted for layers of spherical particles [3].

As another test of the limits of the Born approximation, we examine the resonance-to-resonance transition for $n = 1$, corresponding to the points labeled (1) and (1′) in the right-hand diagrams of Fig. 3, as the modulation amplitude is increased. In Fig. 4 we show the variation of the elastic ($n = 0$) and inelastic $n = 1$ components of the scattering cross section as we increase the modulation amplitude η. We see that the Born approximation is valid at small modulation amplitudes ($\eta \sim 10^{-3}$) but higher-order effects quickly become important as η increases, causing the approximation to fail.

IV. CONCLUSIONS

In summary, within a perturbative framework, we formulated a first-order Born approximation for light scattering by particles with a permittivity that varies periodically in time. By treating the temporal variation as a weak perturbation to an otherwise static particle, as appropriate in practical implementations, we obtained compact expressions for the T matrix that clarify how inelastic scattering amplitudes are governed by overlap integrals between the modes at the input and output frequencies. This insight offers a clear physical interpretation of frequency-conversion processes and directly connects the strength of inelastic channels to the spatial structure and mutual overlap of the underlying static modes.

Using a dielectric sphere as a benchmark system, we demonstrated that the Born approximation quantitatively reproduces dynamic EBCM results for modest modulation amplitudes and accurately captures both enhancement and suppression of inelastic scattering for resonance-to-resonance optical transitions, including sharp dips due to near-orthogonality of radial modes. Extending the analysis to a high-permittivity cylindrical resonator, we showed that geometric tuning of the aspect ratio brings resonances close enough to hybridize, altering their modal overlap and transforming dips in inelastic scattering into prominent peaks.

These results highlight how the spatial structure and mutual overlap of static modes directly govern the strength of inelastic channels and demonstrate that simple geometric or material tuning can selectively suppress or enhance frequency-conversion processes in time-modulated photonic resonators. Moreover, the approach can naturally account for nonuniform refractive index-variations and can be readily incorporated into existing static T matrix formulations to describe scattering from time-modulated scatterers. Overall, this work confirms the predictive power of the perturbative approach, clarifies the central role of mode structure in time-dependent scattering, and provides practical guidance for designing dynamically modulated resonators with tailored frequency-conversion properties.

Future extensions may incorporate higher-order perturbative corrections, explore nonuniform or anisotropic time-variations, and integrate the present formalism into multiple-scattering frameworks to describe complex time-modulated photonic architectures.

Appendix A: Calculation of the volume integral

Using the identity

$$\int_V [\mathbf{a}\cdot(\nabla\times\nabla\times\mathbf{b}) - (\nabla\times\nabla\times\mathbf{a})\cdot\mathbf{b}]\ \mathrm{d}^3r = -\int_{\partial V} \{[\widehat{\mathbf{n}}\times(\nabla\times\mathbf{a})]\cdot\mathbf{b} + (\widehat{\mathbf{n}}\times\mathbf{a})\cdot(\nabla\times\mathbf{b})\}\ \mathrm{d}^2r \tag{A1}$$

and the following properties of vector spherical waves

$$L = p\ell m \Leftrightarrow \widetilde{L} = 1-p, \ell, m, \tag{A2a}$$
$$\nabla \times \mathbf{J}_L(\alpha, \mathbf{r}) = (-1)^p i\alpha \mathbf{J}_{\widetilde{L}}(\alpha, \mathbf{r}), \tag{A2b}$$
$$\nabla \times \nabla \times \mathbf{J}_L(\alpha, \mathbf{r}) = \alpha^2 \mathbf{J}_L(\alpha, \mathbf{r}), \tag{A2c}$$

we obtain

$$\begin{aligned}\int_{V_{\rm in}} &\mathbf{J}_L(\alpha, \mathbf{r}) \cdot \mathbf{J}_{L'}(\beta, \mathbf{r})\, \mathrm{d}^3 r \\ =&\frac{i}{\beta^2-\alpha^2} \int_{\partial V_{\rm in}} \widehat{\mathbf{n}} \cdot \Big\{ (-1)^p \alpha \mathbf{J}_{L'}(\beta, \mathbf{r}) \times \mathbf{J}_{\widetilde{L}}(\alpha, \mathbf{r}) \\ &- (-1)^{p'} \beta \mathbf{J}_L(\alpha, \mathbf{r}) \times \mathbf{J}_{\widetilde{L'}}(\beta, \mathbf{r}) \Big\}\, \mathrm{d}^2 r.\end{aligned} \tag{A3}$$

Introducing the J^+ matrix used in the EBCM [23]

$$J^+_{LL'}(\alpha, \beta) = \alpha\beta \int_{\partial V_{\rm in}} \widehat{\mathbf{n}} \cdot \left[\mathbf{J}_{L'}(\beta, \mathbf{r}) \times \overline{\mathbf{J}}_L(\alpha, \mathbf{r}) \right]\, \mathrm{d}^2 r, \tag{A4}$$

we can rewrite the integral as

$$\begin{aligned}\int_{V_{\rm in}} &\mathbf{J}_L(\alpha, \mathbf{r}) \cdot \mathbf{J}_{L'}(\beta, \mathbf{r})\, \mathrm{d}^3 r \\ &= \frac{i}{\beta^2-\alpha^2} \left\{ \frac{(-1)^m}{\beta} J^+_{\widetilde{L}L'}(\alpha, \beta) - \frac{(-1)^{m'}}{\alpha} J^+_{\widetilde{L'}L}(\beta, \alpha) \right\}.\end{aligned} \tag{A5}$$

Routines to calculate the J^+ matrices are already in use for the EBCM and can be applied straightforwardly.

Appendix B: Born approximation for a sphere - Coefficients and integrals

Setting

$$A = h^+_\ell(q_{\rm h} R) \frac{\partial}{\partial r} \left[r j_\ell(q_{\rm h} r) \right] |_{r=R}, \tag{B1a}$$
$$B = j_\ell(q_{\rm h} R) \frac{\partial}{\partial r} \left[r h^+_\ell(q_{\rm h} r) \right] |_{r=R}, \tag{B1b}$$
$$C = h^+_\ell(q_{\rm h} R) \frac{\partial}{\partial r} \left[r j_\ell(q r) \right] |_{r=R}, \tag{B1c}$$
$$D = j_\ell(q R) \frac{\partial}{\partial r} \left[r h^+_\ell(q_{\rm h} r) \right] |_{r=R}, \tag{B1d}$$

we obtain

$$\alpha_{E\ell}(k) = \frac{qR}{q_{\rm h} R} \varepsilon_{\rm h} \frac{A-B}{C\varepsilon_{\rm h} - D\varepsilon}, \tag{B2}$$

and

$$\alpha_{H\ell}(k) = \mu \frac{A-B}{C\mu_{\rm h} - D\mu}. \tag{B3}$$

We also need to calculate the integral $\int_{V_{\rm in}} \overline{\mathbf{J}}_{L'}(q_{n'}, \mathbf{r}) \cdot \mathbf{J}_L(q_n, \mathbf{r})\, \mathrm{d}^3 r$. The angular integration gives $\delta_{LL'}$, while the radial integration can be performed using the identity [52]

$$\int_0^1 x^2 j_\ell(\alpha x) j_\ell(\beta x)\, \mathrm{d}x = \frac{\beta j_{\ell-1}(\beta) j_\ell(\alpha) - \alpha j_{\ell-1}(\alpha) j_\ell(\beta)}{\alpha^2 - \beta^2}. \tag{B4}$$

Finally we obtain Eq. (28), where

$$D_{E\ell}(\alpha, \beta) = \frac{\alpha j_{\ell-1}(\beta) j_\ell(\alpha) - \beta j_{\ell-1}(\alpha) j_\ell(\beta)}{\alpha^2 - \beta^2} - \ell \frac{j_\ell(\alpha)}{\alpha} \frac{j_\ell(\beta)}{\beta}, \tag{B5}$$

and

$$D_{H\ell}(\alpha, \beta) = \frac{\beta j_{\ell-1}(\beta) j_\ell(\alpha) - \alpha j_{\ell-1}(\alpha) j_\ell(\beta)}{\alpha^2 - \beta^2}. \tag{B6}$$

Therefore, every quantity in Eq. (28) is accessible in a closed form.

[1] F. Morgenthaler, Velocity Modulation of Electromagnetic Waves, IEEE Trans. Microwave Theory Techn. **6**, 167 (1958).

[2] E. Cassedy and A. Oliner, Dispersion relations in time-space periodic media: Part I—Stable interactions, Proc. IEEE **51**, 1342 (1963).

[3] E. Panagiotidis, E. Almpanis, N. Papanikolaou, and N. Stefanou, Optical Transitions and Nonreciprocity in Spatio-Temporally Periodic Layers of Spherical Particles, Advanced Optical Materials **11**, 2202812 (2023).

[4] N. Karl, P. P. Vabishchevich, M. R. Shcherbakov, S. Liu, M. B. Sinclair, G. Shvets, and I. Brener, Frequency Conversion in a Time-Variant Dielectric Metasurface, Nano Lett. **20**, 7052 (2020).

[5] J. L. Valdez-García and P. Halevi, Parametric resonances in a photonic time crystal with periodic square modulation of its permittivity $\varepsilon(t)$, Phys. Rev. A **109**, 063517 (2024).

[6] T. T. Koutserimpas, A. Alù, and R. Fleury, Parametric amplification and bidirectional invisibility in PT - symmetric time-Floquet systems, Phys. Rev. A **97**, 013839 (2018).

[7] M. M. Asgari, P. Garg, X. Wang, M. S. Mirmoosa, C. Rockstuhl, and V. Asadchy, Theory and applications of photonic time crystals: A tutorial, Adv. Opt. Photon.

16, 958 (2024).

[8] L. Yuan, Q. Lin, M. Xiao, and S. Fan, Synthetic dimension in photonics, Optica **5**, 1396 (2018).

[9] S. Mukherjee, M. Di Liberto, P. Öhberg, R. R. Thomson, and N. Goldman, Experimental Observation of Aharonov-Bohm Cages in Photonic Lattices, Phys. Rev. Lett. **121**, 075502 (2018).

[10] E. Galiffi, Y.-T. Wang, Z. Lim, J. B. Pendry, A. Alù, and P. A. Huidobro, Wood Anomalies and Surface-Wave Excitation with a Time Grating, Phys. Rev. Lett. **125**, 127403 (2020).

[11] T. T. Koutserimpas, Extending the Smith-Purcell effect into the fourth dimension, Newton **1**, 100065 (2025).

[12] P. A. Huidobro, E. Galiffi, S. Guenneau, R. V. Craster, and J. B. Pendry, Fresnel drag in space–time-modulated metamaterials, Proc. Natl. Acad. Sci. U.S.A. **116**, 24943 (2019).

[13] C. Caloz and Z.-L. Deck-Léger, Spacetime Metamaterials—Part I: General Concepts, IEEE Transactions on Antennas and Propagation **68**, 1569 (2020).

[14] S. Taravati and A. A. Kishk, Space-Time Modulation: Principles and Applications, IEEE Microwave Magazine **21**, 30 (2020).

[15] E. Galiffi, R. Tirole, S. Yin, H. Li, S. Vezzoli, P. A. Huidobro, M. G. Silveirinha, R. Sapienza, A. Alù, and J. B. Pendry, Photonics of time-varying media, Adv. Photon. **4**, 014002 (2022).

[16] V. Pacheco-Peña, D. M. Solís, and N. Engheta, Time-varying electromagnetic media: Opinion, Opt. Mater. Express **12**, 3829 (2022).

[17] Z. Hayran and F. Monticone, Using Time-Varying Systems to Challenge Fundamental Limitations in Electromagnetics: Overview and summary of applications, IEEE Antennas Propag. Mag. **65**, 29 (2023).

[18] G. Ptitcyn, M. S. Mirmoosa, A. Sotoodehfar, and S. A. Tretyakov, A Tutorial on the Basics of Time-Varying Electromagnetic Systems and Circuits: Historic overview and basic concepts of time-modulation, IEEE Antennas and Propagation Magazine **65**, 10 (2023).

[19] A. Boltasseva, V. M. Shalaev, and M. Segev, Photonic time crystals: From fundamental insights to novel applications: Opinion, Opt. Mater. Express **14**, 592 (2024).

[20] I. Stefanou, P. A. Pantazopoulos, and N. Stefanou, Light scattering by a spherical particle with a time-periodic refractive index, J. Opt. Soc. Am. B **38**, 407 (2021).

[21] K. Schab, B. Shirley, and K. C. Kerby-Patel, Scattering Properties of Spherical Time-Varying Conductive Shells, IEEE Trans. Antennas Propagat. **70**, 7011 (2022).

[22] V. Asadchy, A. Lamprianidis, G. Ptitcyn, M. Albooyeh, Rituraj, T. Karamanos, R. Alaee, S. Tretyakov, C. Rockstuhl, and S. Fan, Parametric Mie Resonances and Directional Amplification in Time-Modulated Scatterers, Phys. Rev. Applied **18**, 054065 (2022).

[23] N. Stefanou, I. Stefanou, E. Almpanis, N. Papanikolaou, P. Garg, and C. Rockstuhl, Light scattering by a periodically time-modulated object of arbitrary shape: The extended boundary condition method, J. Opt. Soc. Am. B **40**, 2842 (2023).

[24] E. Panagiotidis, E. Almpanis, N. Papanikolaou, and N. Stefanou, Inelastic light scattering from a dielectric sphere with a time-varying radius, Phys. Rev. A **106**, 013524 (2022).

[25] R. Soref and B. Bennett, Electrooptical effects in silicon, IEEE J. Quantum Electron. **23**, 123 (1987).

[26] A. Lombardi, M. K. Schmidt, L. Weller, W. M. Deacon, F. Benz, B. De Nijs, J. Aizpurua, and J. J. Baumberg, Pulsed Molecular Optomechanics in Plasmonic Nanocavities: From Nonlinear Vibrational Instabilities to Bond-Breaking, Phys. Rev. X **8**, 011016 (2018).

[27] E. Almpanis, Dielectric magnetic microparticles as photomagnonic cavities: Enhancing the modulation of near-infrared light by spin waves, Phys. Rev. B **97**, 184406 (2018).

[28] D. M. Krichevsky, D. O. Ignatyeva, and V. I. Belotelov, Inverse Faraday effect at Mie resonances, Phys. Rev. Applied **22**, 064087 (2024).

[29] X. Guo, Y. Ding, Y. Duan, and X. Ni, Nonreciprocal metasurface with space–time phase modulation, Light Sci Appl **8**, 123 (2019).

[30] M. Z. Alam, I. De Leon, and R. W. Boyd, Large optical nonlinearity of indium tin oxide in its epsilon-near-zero region, Science **352**, 795 (2016).

[31] S. Saha, O. Segal, C. Fruhling, E. Lustig, M. Segev, A. Boltasseva, and V. M. Shalaev, Photonic time crystals: A materials perspective [Invited], Opt. Express **31**, 8267 (2023).

[32] K. Yee, Numerical solution of initial boundary value problems involving maxwell's equations in isotropic media, IEEE Trans. Antennas Propagat. **14**, 302 (1966).

[33] X. Wang, P. Garg, M. S. Mirmoosa, A. G. Lamprianidis, C. Rockstuhl, and V. S. Asadchy, Expanding momentum bandgaps in photonic time crystals through resonances, Nat. Photon. **19**, 149 (2025).

[34] P. Garg, E. Almpanis, L. Zimmer, J. D. Fischbach, X. Wang, M. S. Mirmoosa, M. Nyman, N. Stefanou, N. Papanikolaou, V. Asadchy, and C. Rockstuhl, Photonic time crystals assisted by quasi-bound states in the continuum (2025), arXiv:2507.15644 [physics].

[35] G. Floquet, Sur les équations différentielles linéaires à coefficients périodiques, Annales scientifiques de l'École Normale Supérieure **12**, 47 (1883).

[36] M. I. Mishchenko, L. D. Travis, and A. A. Lacis, *Scattering, Absorption, and Emission of Light by Small Particles*, 3rd ed. (Cambridge University Press, NASA GISS, 2006).

[37] W. C. Chew, *Waves and Fields in Inhomogenous Media*, IEEE Press Series on Electromagnetic Waves (Wiley-IEEE Press, 1999).

[38] A. Gonis, *Green Functions for Ordered and Disordered Systems*, Studies in Mathematical Physics, Vol. 4 (North-Holland, 1992).

[39] S. Both and T. Weiss, Resonant states and their role in nanophotonics, Semicond. Sci. Technol. **37**, 013002 (2022).

[40] E. Almpanis, N. Papanikolaou, and N. Stefanou, Nonspherical optomagnonic resonators for enhanced magnon-mediated optical transitions, Phys. Rev. B **104**, 214429 (2021).

[41] K. Koshelev and Y. Kivshar, Dielectric Resonant Metaphotonics, ACS Photonics **8**, 102 (2021).

[42] M. M. Sadafi, A. F. da Mota, and H. Mosallaei, Dynamic control of light scattering in a single particle enabled by time modulation, Appl. Phys. Lett. **123**, 101702 (2023).

[43] P. A. Pantazopoulos and N. Stefanou, Layered optomagnonic structures: Time Floquet scattering-matrix approach, Phys. Rev. B **99**, 144415 (2019).

[44] P. A. Pantazopoulos, K. L. Tsakmakidis, E. Almpanis, G. P. Zouros, and N. Stefanou, High-efficiency triple-resonant inelastic light scattering in planar optomagnonic cavities, New J. Phys. **21**, 095001 (2019).

[45] E. Almpanis, G. P. Zouros, P. A. Pantazopoulos, K. L. Tsakmakidis, N. Papanikolaou, and N. Stefanou, Spherical optomagnonic microresonators: Triple-resonant photon transitions between Zeeman-split Mie modes, Phys. Rev. B **101**, 054412 (2020).

[46] M. V. Rybin, K. L. Koshelev, Z. F. Sadrieva, K. B. Samusev, A. A. Bogdanov, M. F. Limonov, and Y. S. Kivshar, High- Q Supercavity Modes in Subwavelength Dielectric Resonators, Phys. Rev. Lett. **119**, 243901 (2017).

[47] P. T. Kristensen, K. Herrmann, F. Intravaia, and K. Busch, Modeling electromagnetic resonators using quasinormal modes, Adv. Opt. Photon. **12**, 612 (2020).

[48] C. Sauvan, T. Wu, R. Zarouf, E. A. Muljarov, and P. Lalanne, Normalization, orthogonality, and completeness of quasinormal modes of open systems: The case of electromagnetism [Invited], Opt. Express **30**, 6846 (2022).

[49] C. Tao, J. Zhu, Y. Zhong, and H. Liu, Coupling theory of quasinormal modes for lossy and dispersive plasmonic nanoresonators, Phys. Rev. B **102**, 045430 (2020).

[50] H. Zhang and O. D. Miller, Quasinormal Coupled Mode Theory (2020), arXiv:2010.08650 [physics].

[51] A. C. Valero, S. Gladyshev, D. Globosits, S. Rotter, E. A. Muljarov, and T. Weiss, Resonant states of structured photonic time crystals (2025), arXiv:2506.01472 [physics].

[52] I. S. Gradshteyn and I. M. Ryzhik, *Table of Integrals, Series and Products*, 7th ed., edited by A. Jeffrey and D. Zwillinger (Academic Press, 2007).